

Chapter 2

Spectroscopy and Microscopy of Graphene Oxide and Reduced Graphene Oxide

Matthew P. McDonald, Yurii Morozov, Jose H. Hodak, and Masaru Kuno

Abstract Graphene oxide (GO) is an important material that provides a scalable approach for obtaining chemically derived graphene. Its optical and electrical properties are largely determined by the presence of oxygen-containing functionalities, which decorate its basal plane. This chemical derivatization results in useful properties such as the existence of a band gap as well as emission spanning both the visible and near infrared. Notably, GO's optical and electrical properties can be altered through reduction, which proceeds through the removal of these oxygen-containing functional groups. However, widely variable behavior has been observed regarding the evolution of GO's optical response during reduction. These discrepancies arise from the different reduction methods being used and, in part, from the fact that nearly all prior measurements have been ensemble studies. Consequently, detailed mechanistic studies of GO reduction are needed which can transcend the limitations of ensemble averaging.

In this chapter, we show the spectroscopic evolution of GO's optical properties during photoreduction at the single-sheet level. Laser-induced reduction, in particular, offers a unique and potentially controllable method for producing reduced GO (rGO), a material with properties similar to those of graphene. However, given the complexity of GO's photoreduction mechanism, microscopic monitoring of the process is essential to understanding and ultimately exploiting this approach.

Keywords Graphene oxide • Reduced graphene oxide • Photolysis • Reduction • Photobrightening • Absorption • Emission • Absorption coefficient • Fluorescence intermittency

M.P. McDonald • M. Kuno (✉)

Department of Chemistry and Biochemistry, University of Notre Dame,
Notre Dame, IN 46556, USA
e-mail: mkuno@nd.edu

Y. Morozov

Department of Physics, Taras Shevchenko National University of Kiev, Kiev, Ukraine

Department of Chemistry and Biochemistry, University of Notre Dame,
Notre Dame, IN 46556, USA

J.H. Hodak

INQUIMAE—Departamento de Química Inorgánica, Analítica y Química Física, Facultad de Ciencias Exactas y Naturales, University of Buenos Aires, Buenos Aires, Argentina

2.1 Graphene, GO, and rGO

2.1.1 Physical Properties of Graphene, GO, and rGO

Since its discovery in the early 2000s [1], graphene has emerged as a major source for exciting new physics and applications. This atomically thin, hexagonal lattice of sp^2 hybridized carbons exhibits many exceptional properties, including optical transparency [2], large carrier mobilities [3], and excellent electrical [4] as well as thermal [5] conductivities. Such properties have led to its use in a variety of applications, such as in transparent/flexible electrodes [6], and in field-effect transistors (FETs) [7].

Many graphene production methods have emerged in recent years [1, 8, 9]. However, for the most part, they remain costly and time consuming. This limits graphene's practical usage. A scalable, low-cost approach for obtaining mass quantities of high-quality graphene is therefore needed.

The chemical oxidation of graphite and its subsequent exfoliation in water result in single-layered GO sheets. In this regard, GO is a promising precursor for chemically derived graphene [10]. Though originally synthesized in 1859 by Brodie [11], a safer, more reliable method for producing graphite oxide was only developed in the 1950s by Hummers and Offeman [12]. Modern methods are essentially slightly modified versions of this synthesis and include a sonication step to exfoliate graphite oxide [10]. Figure 2.1 provides a simplified depiction of how GO is produced today [10], with Chap. 1 of this book providing a more thorough discussion of GO production methods.

Physically, graphene oxide is an atomically thin, semi-aromatic network of sp^2/sp^3 bonded carbon atoms intermittently decorated with oxygen-containing functionalities [13]. These functional groups include hydroxyl (OH), epoxy (C–O–C), carbonyl (C=O), and carboxyl (COOH) species, with OH and C–O–C being the dominant groups across GO's basal plane [13]. Their subsequent removal through disproportionation reactions [14] results in rGO, a chemical analogue of graphene.

GO reduction therefore provides a scalable, low-cost approach for obtaining a graphene-like material [10]. In this regard, reduction can be achieved through various means. They include chemical [15], thermal [16], photothermal [17], and laser-induced [18] reduction methods. All remove GO's oxygen-containing functionalities and simultaneously convert basal plane carbon atoms from sp^3 to sp^2 hybridization, restoring the system's aromaticity to a certain extent.

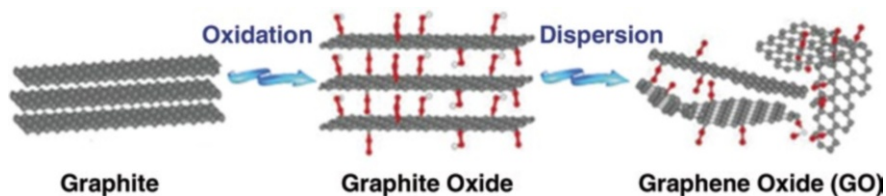


Fig. 2.1 Cartoon illustrating the chemical production of graphene oxide sheets. Reprinted with permission from Zhang Y.L., et al., *Adv. Optical Mater.* **2014**, 2, 10-28. Copyright 2014 Wiley-VCH

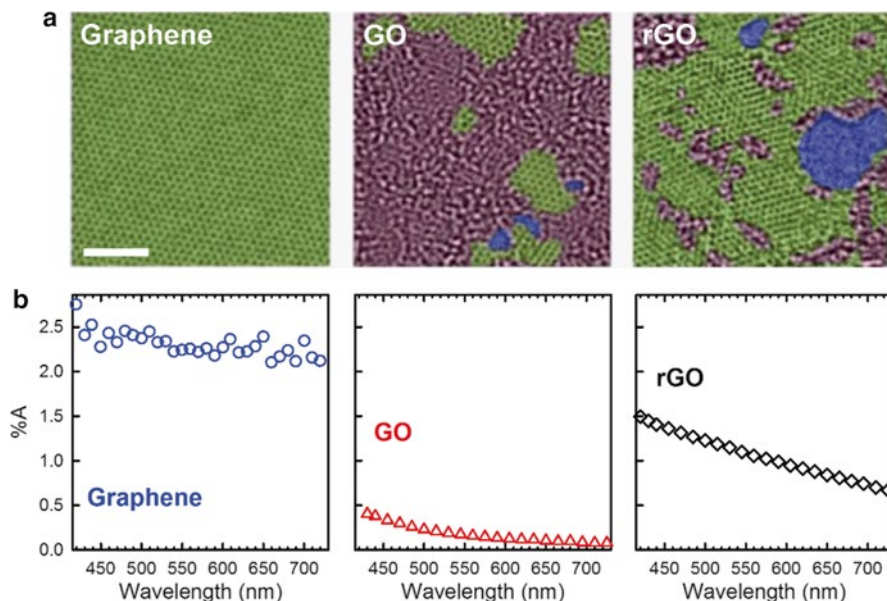


Fig. 2.2 (a) Aberration-corrected TEM images of graphene, GO, and rGO. *Green regions* indicate perfect sp^2 character, *red regions* denote disordered (oxidized) portions, and *blue regions* depict defects/holes. *Scale bar*: 2 nm. Adapted with permission from Erickson K., et al., *Adv. Mater.* 2010, 22, 4467-4472. Copyright 2010 Wiley-VCH. (b) Visible absorption spectra of single-layer graphene (*blue circles*; adapted from ref. [2]), single-layer GO (*red triangles*; adapted from ref. [21]), and single-layer rGO (*black diamonds*; adapted from ref. [21])

To better elucidate the mechanism behind GO to rGO interconversion for possible large-scale production, significant structural characterization has been conducted on these materials at the microscopic level [19, 20]. Electron and tunneling microscopies, in particular, have provided detailed insight into GO's chemical and physical structure. As an illustration, Fig. 2.2a shows high-contrast aberration-corrected transmission electron microscopy (TEM) images of pristine graphene, GO, and rGO [19]. In these micrographs, sp^2 regions are colored green, disordered (oxidized) sp^3 regions are shown in red, and defects/holes are highlighted in blue [19]. These images show that GO clearly regains much of its sp^2 character upon reduction and begins to resemble graphene. However, oxidized regions still exist within rGO and are accompanied by the presence of holes and defects.

These TEM measurements [19]—along with scanning tunneling microscopy (STM) [20] experiments—also show sizable oxygen functionality and sp^2 size distribution heterogeneities within GO and rGO. GO/rGO's oxygen-containing functionalities are additionally observed to be dynamic. Namely, under electron beam irradiation, they migrate across GO/rGO's basal plane [19]. This, coupled with rGO's imperfect/defective structure, highlights the complicated chemistry underlying GO-to-rGO interconversion. Consequently, detailed studies of GO's deoxygenation mechanisms are needed to fully realize its immense potential as a graphene precursor.

2.1.2 Optical Properties of Graphene, GO, and rGO

GO's optical properties are significantly different from those of graphene. Graphene is a zero-gap semiconductor, which possesses a significant, near-constant absorption across the visible ($\sim 2.3\%$ absorption, %A, first panel, Fig. 2.2b) [2]. By contrast, GO's optical absorption is nearly an order of magnitude smaller ($\sim 0.3\%$ A, second panel, Fig. 2.2b) [21, 22]. Furthermore, GO's absorption spectrum is wavelength dependent; it peaks in the UV/blue edge of the visible spectrum and falls towards the near infrared (NIR). Discernible $\pi-\pi^*$ and $n-\pi^*$ transitions are also present in its UV absorption (200–320 nm) and arise from the presence of oxygen-containing functionalities [23, 24]. GO's optical response is thus exquisitely sensitive to its degree of oxidation [25]. As an illustration, the last two panels in Fig. 2.2b show that GO's absorption dramatically increases across the visible upon the removal of these functionalities and approaches graphene's 2.3 %A limit [21, 26].

An additional difference from graphene is that, upon absorbing UV or visible light, GO fluoresces [23, 24, 27–30]. Two broad (200–300 nm full width at half maximum, fwhm) peaks are often observed, centered in the blue (400–500 nm) and red (600–700 nm) regions of the visible spectrum [27, 31]. The origin of this emission is debated. Conventional wisdom suggests that it arises from carrier recombination in isolated/confined sp^2 clusters where varying domain sizes lead to a distribution of energy gaps that results in a spectrally broad emission [31]. However, quasi-molecular transitions and even heterogeneous carrier relaxation kinetics have been invoked to explain its origin and appearance [28, 29]. In the former case, intriguing evidence for quasi-molecular photoluminescence, arising from basal plane oxygen-functionalized aromatic clusters, has been observed in GO excitation spectra [29]. In the latter case, optical Kerr-gate photoluminescence measurements have revealed clear spectral dynamics following excitation. Specifically, GO's emission redshifts from 460 to 690 nm over the course of ~ 10 ps following excitation and clearly indicates the existence of heterogeneous carrier relaxation kinetics [28].

Next, GO's emission changes gradually upon reduction. However, as with its native emission, the literature is replete with differences in reported behavior. In this regard, GO/rGO's emission has been reported to blueshift [27], redshift [30], or not shift at all [23] from GO's initial spectrum during reduction. To illustrate, Fig. 2.3a shows the emission spectrum of a GO suspension during Xe arc lamp photoreduction [27]. The initial spectrum (solid red line) exhibits GO's characteristic red (~ 600 nm) and blue (~ 500 nm) peaks, with the red portion dominating. As reduction progresses, the red peak disappears while the blue feature begins to dominate, ultimately leading to an effective blueshift of the spectrum.

By contrast, Fig. 2.3b shows seemingly contradictory behavior during GO's *chemical* (i.e., hydrazine) reduction. Namely, its emission spectrum redshifts from ~ 700 to ~ 850 nm upon reduction [30]. Adding to the confusion, other studies have shown no discernible shift in GO's emission spectrum upon hydrazine reduction (Fig. 2.3c) [23].

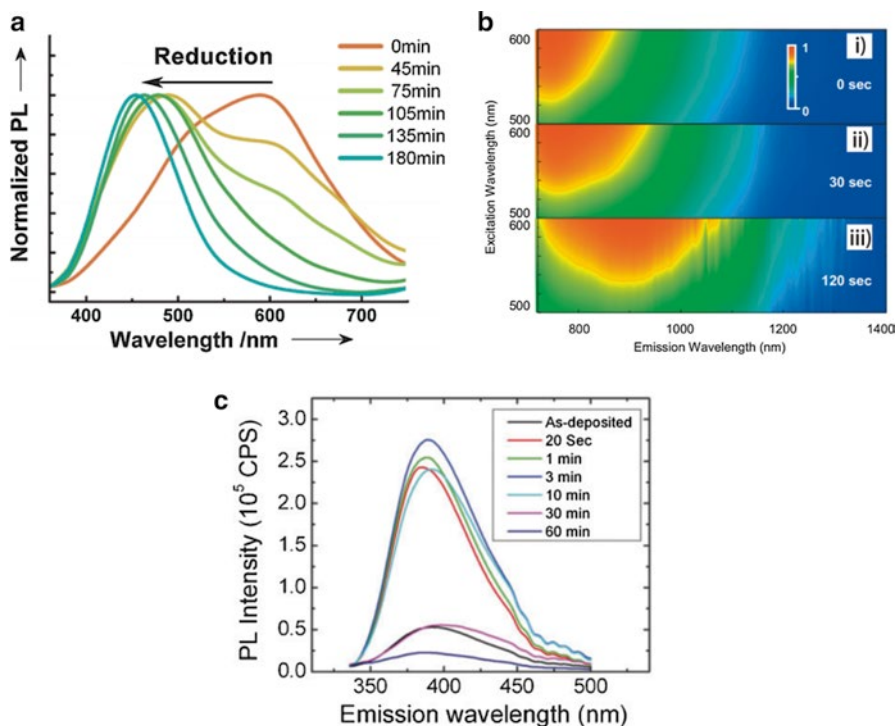


Fig. 2.3 (a) Normalized photoluminescence (PL) spectra of GO suspensions during photoreduction. Reprinted with permission from Chien C-T, et al., *Angew. Chem. Int. Ed.*, 2012, 51, 6662–6666. Copyright 2012 Wiley-VCH. (b) Normalized PL excitation-emission maps of GO during chemical reduction. Reprinted with permission from Luo Z., et al., *Appl. Phys. Lett.*, 2009, 94, 111909. Copyright 2009 AIP. (c) PL spectra of GO thin films during chemical reduction. Reprinted with permission from Eda G., et al., *Adv. Mater.*, 2010, 22, 505–509. Copyright 2010 Wiley-VCH

Table 2.1 highlights these differences by compiling characteristic features of literature-reported GO/rGO emission spectra observed during reduction. The table is grouped by reduction method. Widely varying responses are seen depending on sample type (suspensions, solid films, or single sheets) and/or reduction method. However, no clear correlation exists between the observed spectral response and reduction method. Additionally, chemical reduction (hydrazine, in particular) appears to contribute most to the variability of the observed behavior.

This variability and lack of consensus stem, in part, from the fact that the vast majority of GO/rGO optical studies have been conducted at the ensemble level [15–17, 23–31, 36]. Consequently, to begin resolving these discrepancies single-GO/rGO sheet optical measurements, which transcend ensemble averaging, are needed to reveal the microscopic photophysics underlying GO-to-rGO interconversion [32, 37].

Table 2.1 Comparison of GO and rGO emission properties during GO-to-rGO interconversion

Sample type	λ_{exc} (nm)	GO spectrum; max (nm)	Reduction method	rGO spectrum; max	References
Susp.	325	DP; 600	PT (Xe lamp)	SP; 450 nm (blueshift)	[27]
Film	400	DP; 690	PT (Xe lamp)	SP; 460 nm (blueshift)	[28]
Sing.	473	SP; 700	L (473 nm)	SP; 625 nm (blueshift)	[32]
Sing.	405	DP; 690	L (405 nm)	SP; 500 nm (blueshift)	[33]
Film	488	SP; 650	Hydrazine	MP; 700–900 nm (redshift)	[30]
Film	325	SP; 390	Hydrazine	SP; 390 nm (no shift)	[23]
Film	325	MP; 500–700	Hydrazine	MP; 530 nm (blueshift)	[34]
Film	325	MP; 500–700	T (700 °C)	MP; 500–700 nm (slight blueshift)	[34]
Susp.	<500	SP; 650	T (120 °C)	SP; 475 nm (blueshift)	[35]

λ_{exc} excitation wavelength, *Susp.* suspension, *Sing.* single sheet, *SP* single peak, *DP* double peak, *MP* multiple peaks, *PT* photothermal, *L* laser, *T* thermal

2.2 Single-GO Sheet Absorption Microscopy/Spectroscopy

To investigate the optical properties of individual GO and rGO sheets as well as their intrasheet optical properties, we have recently developed a unique toolset to probe both the spatially resolved absorption and emission of individual single-layer GO/rGO specimens [21, 33]. When these measurements are carried out before, during, and after photolytic GO reduction, they provide an unprecedented look at how GO's optical properties evolve throughout its reduction process.

These measurements are part of a broader class of studies we have conducted to probe the photophysics of individual nanostructures [38–42]. Examples include CdSe nanowires [38–42], single-walled carbon nanotubes [42], and Au nanoparticles [42]. Notably, the implementation of single-particle *absorption* microscopy/spectroscopy is unique to our approach and serves to broaden the scope of traditional emission-based single-molecule/particle techniques. In this respect, not all specimens are emissive or possess sizable emission quantum yields (QY). Hence, these materials are inaccessible to current single-particle microscopies.

To acquire single-GO/rGO sheet absorption images and spectra, three diode lasers (405, 520, and 640 nm; Coherent) and a broadband supercontinuum laser (Fianium) are used. Figure 2.4 shows a schematic of the optical setup built to conduct these experiments. The entire system is constructed around an inverted microscope (Nikon) that supports a 3-axis closed-loop piezo positioner (Mad City Labs) and a 2-axis manual micrometer stage (Semprex). GO suspensions are prepared using a modified Hummers synthesis [33]. Optical samples are then made by drop casting dilute suspensions onto fused silica coverslips (Esco) which are then affixed to the piezo stage. This enables precise control of the sample's position. As-prepared samples generally consist of ~90 % single-layer GO sheets [33].

Figure 2.4 shows the optical path of the excitation source. Prior to entering the microscope, each laser is split into signal and reference beams. The signal beam

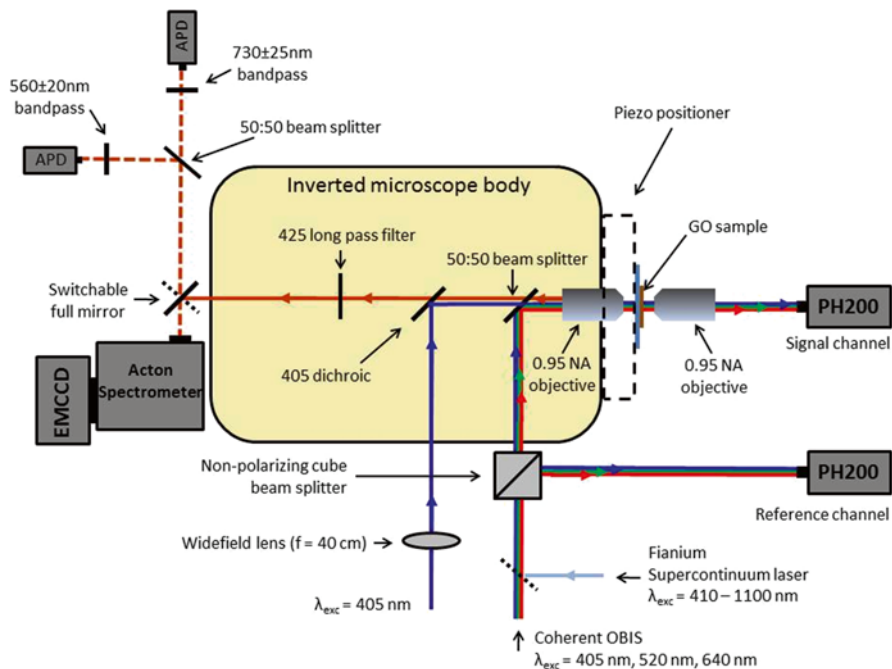


Fig. 2.4 Optical setup for spatially resolved absorption and emission imaging/spectroscopy

is focused onto samples by way of a high NA microscope objective (Nikon 0.95). The reference beam is simultaneously focused onto a near-shot noise-limited photodetector (Highland Technologies, PH200). Light transmitted through the sample is then collected by a second, collinear, high NA objective (Nikon 0.95) and is focused onto an identical PH200 photodetector. Typical excitation intensities (I_{exc}) are $I_{\text{exc}} \sim 150 \text{ Wcm}^{-2}$. To mitigate laser power fluctuations, the transmitted signal is normalized by the reference detector's voltage.

Spatially resolved absorption images of a single GO/rGO sheet are constructed by raster-scanning the specimen through the probe laser's focus and monitoring the transmitted light intensity (I) point by point. The associated incident intensity (I_0) is obtained by averaging over a region of the image free of absorbing species. This allows the transmittance ($T = I/I_0$) or % absorption [%A = $(1 - T) \times 100$] to be quantified for every pixel (an approximate $250 \text{ nm} \times 250 \text{ nm}$ region). The sample's absorption coefficient (α ; cm^{-1}) is then obtained using [21]

$$\alpha \left(\text{cm}^{-1} \right) = \frac{-\ln \left(1 - \frac{\%A}{100} \right)}{x \text{ (cm)}} \quad (2.1)$$

where we assume a specimen thickness, x (cm), of 1 nm (1×10^{-7} cm) [20]. Typical detection limits for these measurements are ~ 0.02 – 0.06 %A and are limited by laser noise, consistent with mode hopping [21].

Corresponding absorption spectra are acquired by dispersing the output of the supercontinuum laser with an acousto-optic tunable filter (AOTF, effective range 410–800 nm). To limit laser exposure during absorption measurements—thereby minimizing photo-induced changes in the specimen—the probe is pulsed once for 3 ms at each point. The transmitted pulse is then digitized, fast Fourier transformed (FFT), and low pass filtered to remove any high-frequency noise. Additional information about the approach can be found in ref. [21].

Figure 2.5 shows resulting absorption images of a representative single GO sheet acquired at (a) 405 nm, (b) 520 nm, and (c) 640 nm. Measured %A-values for this particular sheet are ~0.68 % (405 nm), ~0.25 % (520 nm), and ~0.13 % (640 nm). Corresponding α -values (evaluated using Eq. 2.1) are $\alpha_{405} = 6.8 \times 10^4 \text{ cm}^{-1}$, $\alpha_{520} = 2.5 \times 10^4 \text{ cm}^{-1}$, and $\alpha_{640} = 1.3 \times 10^4 \text{ cm}^{-1}$. Interestingly, individual sheets show varying α -value distributions (Fig. 2.5a–c; green and blue histograms) as compared to an ensemble distribution composed of 12 individual sheets (Fig. 2.5a–c; gray histograms). This indicates that intersheet absorption heterogeneities exist, which likely stem from sheet-to-sheet variations in their extent of oxidation.

From the images, it is also apparent that there are significant *intrasheet* absorption efficiency differences at each wavelength. Some regions absorb more of a given color than other regions. This is highlighted, for example, by the upper left portion of the sheet profiled in Fig. 2.5a where one sees a large $\sim 1 \mu\text{m}^2$ region having ~ 0.9 %A. This value is ~ 0.2 %A higher than the rest of the sheet. Other regions exhibit varied absorption efficiencies and are readily apparent in Fig. 2.5a–c. An implication of these results is that chemically segregated regions on the $\sim \mu\text{m}^2$ scale exist within GO's basal plane. These results are not unique and are observed in all single-layer GO sheets we have studied.

Consequently, extracted %A parameters, averaged over 12 individual GO sheets, are 0.6 ± 0.1 %, 0.21 ± 0.04 %, and 0.11 ± 0.03 % at 405 nm, 520 nm, and 640 nm, respectively. Corresponding α -values are $\alpha_{405} = 6 \pm 1 \times 10^4 \text{ cm}^{-1}$, $\alpha_{520} = 2.1 \pm 0.4 \times 10^4 \text{ cm}^{-1}$, and $\alpha_{640} = 1.1 \pm 0.3 \times 10^4 \text{ cm}^{-1}$. To put these numbers into context, graphene possesses an approximate α -value of $\alpha = 5.8 \times 10^5 \text{ cm}^{-1}$ across the visible [evaluated using Eq. (2.1) by assuming a thickness of 0.4 nm (4×10^{-8} cm) and %A=2.3 %] [2, 43].

At this point, given that our approach enables the visible spectrum of single-layer GO to be acquired, estimates of GO's full wavelength-dependent absorption coefficient can be made. To illustrate, Fig. 2.5d shows the absorption spectrum of a single GO sheet in green triangles. Average α -values from 12 single-sheet absorption images are also shown (blue circles). Superimposed over the single-sheet data is the corresponding ensemble absorption spectrum (dashed red line). Both spectra qualitatively agree, showing a monotonic increase of the absorption as one moves to progressively blue wavelengths. By fitting the single-sheet data, an equation, which provides an estimate for GO's wavelength-dependent α -value between $\lambda = 450$ –700 nm, is

$$\alpha \left(\text{cm}^{-1} \right) = 665,000 - \lambda (2,970) + \lambda^2 (4.54) - \lambda^3 \left(2.35 \times 10^{-3} \right). \quad (2.2)$$

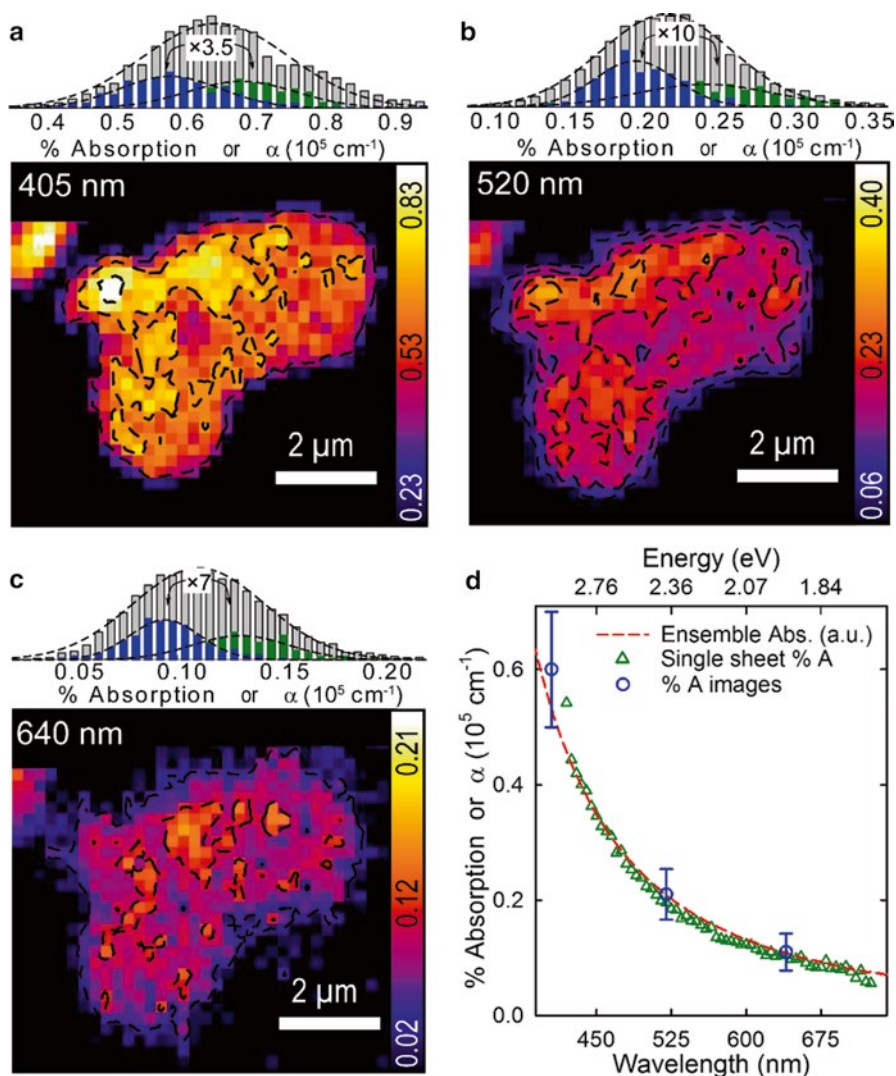


Fig. 2.5 Absorption images of single-layer GO acquired at (a) 405 nm (contour interval, 0.2 % absorption), (b) 520 nm (contour interval, 0.05 % absorption), and (c) 640 nm (contour interval, 0.05 % absorption). The *false color scale* represents %A. *Gray histograms* above each image show the %A (and corresponding α -value) distribution for a 12-sheet GO ensemble. *Green and blue histograms* represent the %A distribution for two separate sheets. (d) Absorption spectrum for a single GO sheet (*green triangles*) compared to its parent ensemble absorption spectrum (*red dashed line*) and to single λ absorption images (*blue circles*). Reprinted with permission from Sokolov, D.A., et al., *Nano Letters* 2014, 14, 3172–3179. Copyright 2014 American Chemical Society

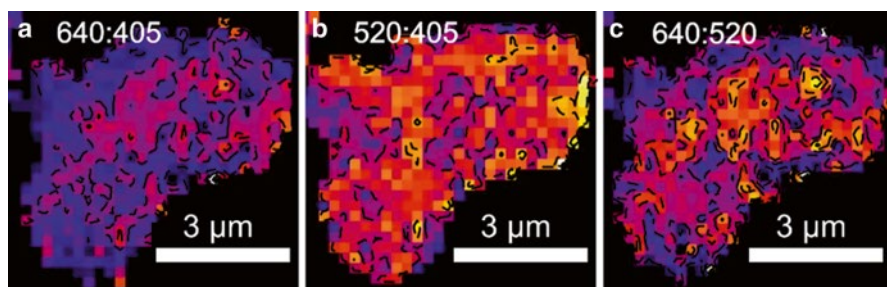


Fig. 2.6 Absorption ratio maps of the same GO sheet featured in Fig. 2.5. Wavelength ratios are (a) 640 nm:405 nm, (b) 520 nm:405 nm, and (c) 640 nm:520 nm. The false color scale represents ratio values, where yellow/white is high and blue/black is low. Reprinted with permission from Sokolov, D.A., et al., *Nano Letters* 2014, 14, 3172–3179. Copyright 2014 American Chemical Society

Intrasheet absorption heterogeneities can be further explored by constructing ratios of absorption images obtained at different colors. This, in turn, provides a sense for intrasheet *spectral* heterogeneities present in the sample. Figure 2.6 shows examples of such absorption ratio maps for the same GO sheet featured in Fig. 2.5. In particular, Fig. 2.6a is the resulting ratio image obtained by dividing the sheet’s 640 nm image with its 405 nm counterpart. Likewise, Fig. 2.6b, c results from dividing the sheet’s 520 nm image with its 405 nm counterpart and its 640 nm image with its 520 nm counterpart. These images show ratio values which are not constant across the specimen. Consequently, they indicate that spectral heterogeneities exist within the sheet. This likely stems from variations in sp^2 domain sizes and chemical heterogeneities that favor a disordered electronic energy gap distribution [24, 27]. Ratio maps for other GO sheets show identical intrasheet heterogeneities and can be found in ref. [21].

2.3 Single-GO Sheet Emission Microscopy/Spectroscopy

Next, the instrument we have built (Fig. 2.4) supports emission imaging through either standard widefield imaging techniques or confocal scanning microscopy. In both cases, single-layer GO samples are excited with a 405 nm continuous wave (CW) laser diode passed through a high NA objective (Nikon 0.95). The resulting emission can then be studied to more fully elucidate GO’s spatial and spectral characteristics.

For widefield imaging, an $f=40$ cm lens is placed in the excitation path so that the laser comes to a focus just prior to the objective’s back focal plane. This results in a large (~ 30 μm) excitation area with a corresponding excitation intensity of $I_{\text{exc}} \sim 300$ Wcm^{-2} . Emission is collected through the same objective and is passed through a 405 nm dichroic filter (Semrock) and a 425 nm long-pass filter (Chroma).

This light is then focused onto the entrance slit of an imaging spectrometer (Acton) that contains a 50 g/mm (600 nm blaze) grating. An electron-multiplied CCD camera (EMCCD, Andor), positioned at the exit of the spectrometer, acquires both emission images and spectra.

For confocal measurements, the collimated laser is passed directly into the objective and results in a diffraction-limited spot at the focus ($I_{\text{exc}} = 150 \text{ Wcm}^{-2}$). A piezo positioner raster scans the sample relative to the laser focus with dwell times per pixel below 1 s so as to minimize laser-induced changes in the sample. Emission is collected using the same focusing objective and is passed through a 405 nm dichroic filter (Semrock) and a 425 nm long-pass filter (Chroma). The emission is then collimated, split into two channels, and focused through two separate band-pass filters (Chroma: $730 \pm 25 \text{ nm}$; $560 \pm 20 \text{ nm}$) onto identical single-photon counting avalanche photodiodes (APD; Perkin Elmer).

Figure 2.7 shows an emission spectrum obtained from a $\sim 2 \mu\text{m}$ wide strip of a single GO sheet. Two characteristic peaks are observed, located in the blue ($\sim 490 \text{ nm}$) and red ($\sim 690 \text{ nm}$) portions of the visible spectrum. This agrees with other reported ensemble GO spectra [27–29]. As described earlier, GO's broad emission is generally attributed to various causes including the presence of intra-sheet sp^2 domain size distributions [24, 27], quasi-molecular ligand/ sp^2 states [29], and heterogeneous carrier relaxation kinetics [28]. Associated single-GO sheet emission QYs—determined from correlated absorption/emission measurements—are on the order of $\sim 1 \%$ [21].

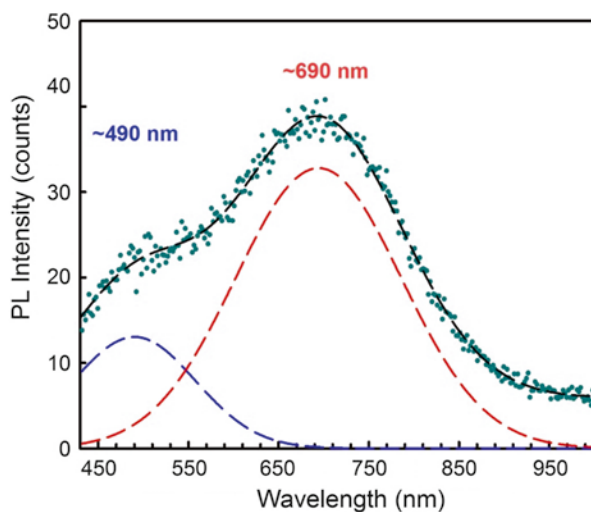


Fig. 2.7 Emission spectrum of a single GO sheet (solid green circles) showing both blue and red components. The trace is fit to a sum of Gaussians (dashed black line) where two individual components (dashed blue and red lines) are extracted with center wavelengths of ~ 490 and $\sim 690 \text{ nm}$. Traces offset for clarity. Reprinted with permission from McDonald, M.P., et al., *Nano Letters*, 2013, 13, 5777–5784. Copyright 2013 American Chemical Society

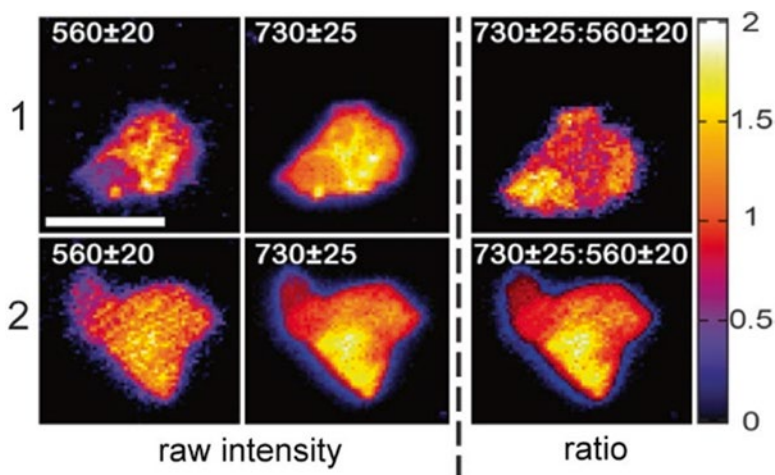


Fig. 2.8 Confocal emission images of two different (rows 1 and 2) GO sheets under 405 nm excitation. In either case, the collected emission is split into *red* (730 ± 25 nm) and *green* (560 ± 20 nm) channels using band-pass filters (corresponding raw intensity images are to the left of the dashed line). The rightmost column shows ratio images of the two colors ($730 \pm 25:560 \pm 20$). Scale bar: $5 \mu\text{m}$. Reprinted with permission from McDonald, M.P., et al., *Nano Letters*, 2013, 13, 5777–5784. Copyright 2013 American Chemical Society

As with earlier single-sheet absorption images, single-sheet confocal emission maps exhibit substantial spatial heterogeneities. Figure 2.8 illustrates this with two sets of representative confocal images obtained in the green (560 ± 20 nm) and red (730 ± 25 nm) portions of the GO spectrum. Intensity variations exist in each image indicating that different parts of the same sheet emit different amounts of the same color. To illustrate, the lower left portion in Fig. 2.8(1) is much less emissive than the rest of the sheet. This could stem from local emission QY variations, spectral differences, or associated absorption heterogeneities. Correlated absorption/emission images, however, show no apparent link between absorption and emission magnitudes. Consequently, absorption heterogeneities (e.g., Fig. 2.5) alone do not account for the observed intensity variations in Fig. 2.8 [21]. Local emission efficiencies can be determined using spatially resolved emission lifetime experiments. However, such studies have not been conducted yet and are reserved for future investigations.

At this point, to reveal the existence of any intrasheet emission spectral differences, ratio maps are created by dividing single-color, confocal images (right column, $730 \pm 25:560 \pm 20$). Resulting maps indicate the existence of significant intrasheet spectral heterogeneities which can be seen as bright and dim domains in the representative images shown in Fig. 2.8. Namely, the GO sheet in Fig. 2.8(1) possesses a large ($\sim 1 \mu\text{m}^2$) portion that emits primarily red light (bottom left of sheet). The rest of the sheet emits predominantly green light. Similar spectral heterogeneities exist in other GO sheets, with a second example shown in Fig. 2.8(2). We find no specific trends in the location of these predominantly red- or green-emitting regions, whether at the

edges or the center of the sheets. Analogous spatial and spectral heterogeneities appear when using images acquired with other red and blue wavelengths [33].

The spatially heterogeneous emission spectrum of single-layer GO resembles analogous absorption spectral heterogeneities shown earlier in Fig. 2.6. This further demonstrates that significant disorder exists in the optical response of single-layer GO, stemming from the presence of sp^2 domain size distributions as well as associated chemical heterogeneities.

2.4 GO Photoreduction

Having established the intrinsic absorption and emission optical response of single-layer GO, we now investigate their evolution during reduction. In particular, we find that GO's photophysical properties change when individual sheets are exposed to prolonged periods of widefield 405 nm laser excitation [33, 21]. We observe what appear to be three distinct behaviors (called "Regions" in what follows) that characterize GO's optical evolution. This is illustrated in Fig. 2.9a where the top and bottom rows show correlated absorption and emission images of a single-layer GO sheet during continuous 405 nm irradiation ($I_{\text{exc}} \sim 220 \text{ Wcm}^{-2}$) [21]. Three pairs of images depict GO's absorption/emission prior to irradiation, after exposure for 55 s, and after exposure for 1,390 s of 405 nm irradiation.

From the images, GO's absorption and emission are seen to readily evolve. The most notable changes seen are the overall increase (decrease) of its absorption (emission). To better illustrate these changes, though, Fig. 2.9b shows the time-dependent evolution of GO's absorption/emission, extracted from a single point on the sheet (circled). Extending these measurements to all pixels subsequently reveals corresponding spatially resolved intrasheet absorption/emission differences which will be described in more detail below.

From Fig. 2.9, it is apparent that GO's initial response upon irradiation (denoted Region 1 in what follows) is a significant drop in emission intensity with a concomitant rise in absorption magnitude. Specifically, within the first 55 s of exposure to 405 nm light the emission intensity decreases by an order of magnitude with a corresponding quantum yield (QY) change from 0.65 to 0.075 % [21]. The total associated 405 nm photon dose (Φ) yielding this change is $\Phi = 2.5 \times 10^{22}$ photons/cm²

[$\Phi = I_{\text{exc}} \times \left(\frac{\lambda}{hc} \right) \times t$ where λ is the excitation wavelength, h is Planck's constant, c is the speed of light in a vacuum, and t is the exposure time]. In parallel, Fig. 2.9c shows that this drop in emission intensity is accompanied by a simultaneous ~ 190 nm blueshift of the spectrum. A corresponding rise in absorption leads to a change in GO's 520 nm absorption efficiency from ~ 0.2 %A at the start of the experiment to ~ 1.3 %A.

Beyond ~ 100 s of exposure to 405 nm light ($\Phi = 4.5 \times 10^{22}$ photons/cm²), Fig. 2.9b shows that this trend reverses. In what follows, this behavior is referred to as Region 2 of GO's optical evolution (denoted by the shaded blue region in Fig. 2.9b).

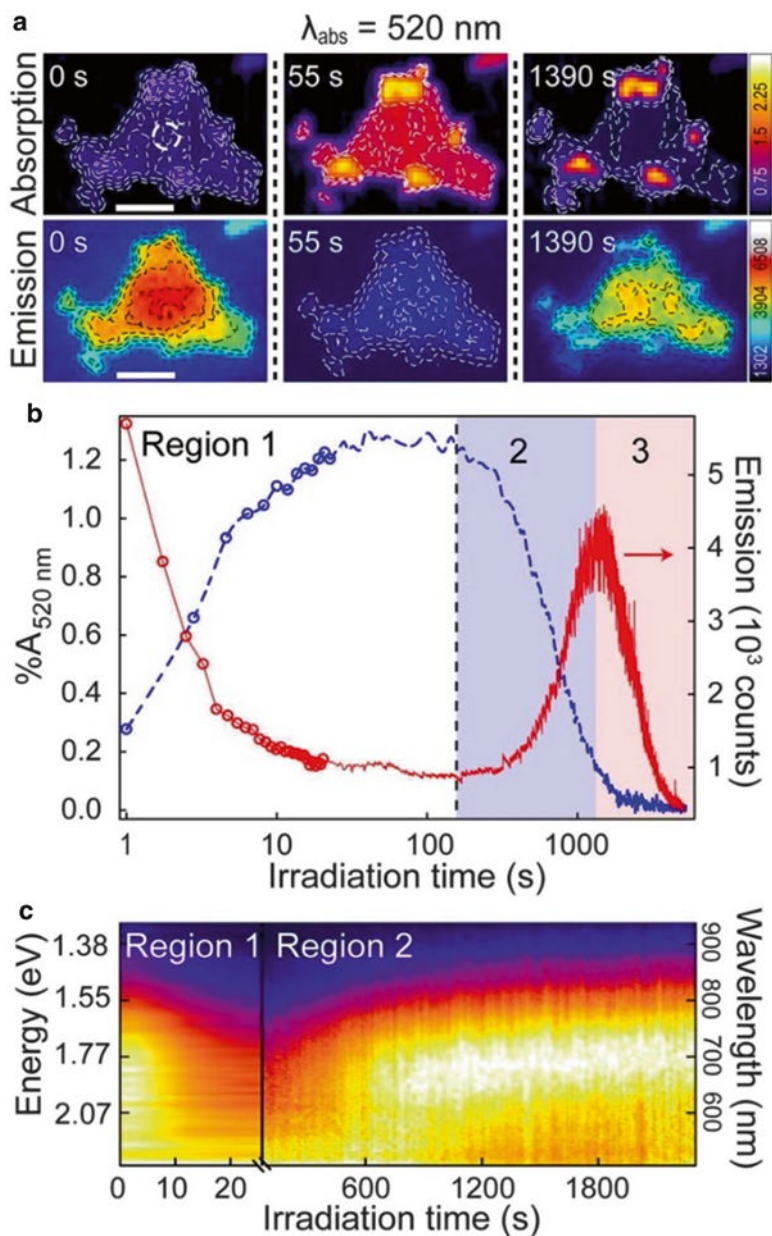


Fig. 2.9 (a) Correlated absorption/emission images acquired during single-layer GO reduction ($\lambda_{\text{abs}}=520 \text{ nm}$). Scale bar: $3 \mu\text{m}$. (b) Absorption (dashed red line/circles) and emission (solid blue line/circles) intensities as a function of exposure time for the sheet featured in (a) where shaded/colored portions reflect Regions 1, 2, and 3. (c). Waterfall plot of a sheet's normalized emission spectrum throughout Regions 1 and 2. Reprinted with permission from Sokolov, D.A., et al., *Nano Letters* 2014, 14, 3172–3179. Copyright 2014 American Chemical Society

Namely, we observe that the sheet's emission brightens with emission QYs increasing from ~ 0.075 to 14 % [21]. A corresponding spectral redshift to ~ 725 nm (Fig. 2.9c) also occurs. At the same time, the sheet's absorption decreases by an order of magnitude, falling from a peak of ~ 1.3 to ~ 0.17 %.

Beyond this, there exists a third region of GO's optical response (called Region 3 and denoted by the shaded pink region in Fig. 2.9b) where both the emission and absorption decrease together. In the emission, we observe clear episodes of emission intermittency (i.e., intensity fluctuations that are not shot noise or laser intensity related) before irreversible photobleaching. In the absorption, the absorption efficiency continues to drop and eventually falls below the instrument's detection limit (~ 0.03 %A).

These correlated absorption/emission images have been acquired as follows. In brief, an absorption image is first taken and is then immediately followed by a 0.5–2-s period of widefield 405 nm laser exposure ($I_{\text{exc}} \sim 220$ W cm $^{-2}$). Emission images are obtained during this time with an EMCCD camera. This absorption/emission imaging sequence is then repeated until no additional changes are seen in either the sheet's absorption or emission. This is referred to as the "stepwise" reduction method in the following discussions. Stop motion absorption/emission movies are subsequently created using these sequential images and can be found in ref. [21]. In this way, the spatial evolution of GO's optical properties has been mapped out throughout its optical life cycle.

An initial hypothesis for these observations is that they are linked to light-induced GO reduction. Supporting this, Fig. 2.9 shows that at the end of Region 1 the specimen's emission is weak and is blueshifted compared to that of pristine GO [28, 31]. Furthermore, the sample's absorption magnitude approaches that of graphene ~ 2.3 % [2]. This then suggests that prolonged 405 nm irradiation reduces GO and yields rGO at the end of Region 1. Continued light-induced chemistry then occurs in Region 2, causing rGO's emission to increase and its absorption to decrease. Loss of *both* the absorption and emission in Region 3 suggests that rGO is eventually destroyed.

To solidify this hypothesis and, in particular, the claim that Region 1 represents the photoreduction of GO to rGO, we probe the chemical nature of this transformation at the ensemble level using ensemble absorption spectroscopy, chemically specific X-ray photoelectron spectroscopy (XPS), Fourier transform infrared (FTIR) spectroscopy, and bulk electrical transport measurements.

To carry out these studies, an ensemble sample was prepared by irradiating a high-concentration, aqueous GO suspension with 405 nm light ($I_{\text{exc}} \sim 0.2$ W cm $^{-2}$) for 16.5 h. The associated photon dose is $\Phi \sim 2 \times 10^{22}$ photons/cm 2 and is equivalent to ~ 30 s of 405 nm laser exposure in the single-sheet experiment. This places the ensemble sample close to the end of Region 1 where we have claimed that rGO exists based on the single-sheet results in Fig. 2.9 [33].

Figure 2.10a first shows results of the ensemble absorption experiment where we see that GO's absorption gradually increases over the course of irradiation. The inset in Fig. 2.10a better illustrates this, revealing a near-linear rise in absorption at 405 nm. This change is accompanied by a noticeable decrease of the

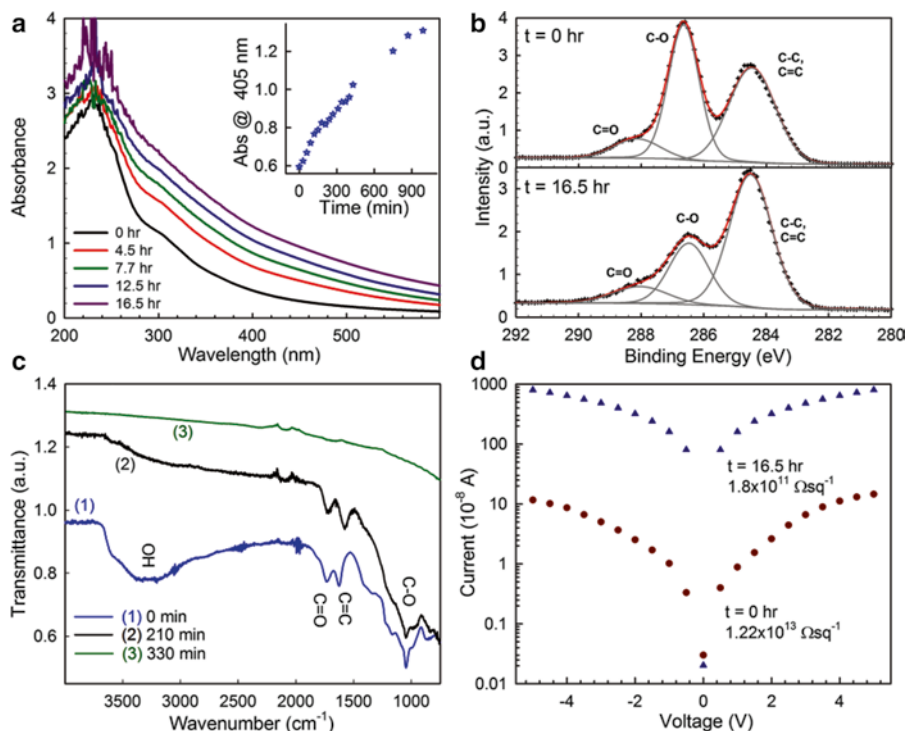


Fig. 2.10 Ensemble GO/rGO measurements. (a) Absorption spectra of an aqueous suspension of GO throughout exposure to 16.5 h (990 min) of 0.2 Wcm^{-2} 405 nm light (*inset*: absorption values at 405 nm as a function of irradiation time). (b) XPS C1s spectra of the GO ensemble before (*top*) and after (*bottom*) exposure to 16.5 h of 0.2 Wcm^{-2} 405 nm light. (c) FTIR spectra of a GO film (1) exposed to 220 min (2) and 330 min (3) of 2 Wcm^{-2} 405 nm laser irradiation. (d) Transport measurements of a GO ensemble before (*red circles*) and after (*blue triangles*) exposure to 16.5 h of 0.2 Wcm^{-2} 405 nm light

$n-\pi^*$ resonance at $\sim 320 \text{ nm}$, which is an observation consistent with earlier literature studies [23].

Next, Fig. 2.10b shows corresponding XPS spectra of the same ensemble. Chemical specificity in the measurement and specifically the ability to determine a sample's oxygen content come from the binding energy shift experienced by carbon 1s (C1s) electrons in the presence of bound oxygen [44]. In our study, probing the C1s photoelectron spectrum reveals that peaks associated with oxidized carbon [44] substantially diminish after 16.5 h of exposure to 405 nm irradiation. Extracted estimates of the carbon-carbon/carbon-oxygen bond ratios (C:O) before and after 405 nm irradiation are 0.85 and 1.7, respectively. This indicates loss of oxygen during irradiation and supports the light-induced reduction of GO.

Additional, chemically specific evidence for reduction comes from associated FTIR spectra, obtained at given intervals during 405 nm irradiation ($I_{\text{exc}} \sim 2 \text{ Wcm}^{-2}$).

In this case, a dried GO film was used instead of the suspension to mitigate background OH vibrations associated with water. FTIR spectra in Fig. 2.10c show that IR transitions associated with GO's oxygen-containing functionalities all but disappear after 5.5 h of irradiation ($\Phi \sim 6 \times 10^{22}$ photon/cm²) [33]. These FTIR results clearly show that OH species are the first to be removed and are consistent with their basal plane abundance as well as with prior literature results [45, 46].

Finally, associated two-probe transport measurements of thin films made using these GO ensembles (Fig. 2.10d) show a sharp decrease in sheet resistance as a function of 405 nm irradiation. Specifically, experimental in-plane resistances drop nearly two orders of magnitude, falling from $\sim 1.2 \times 10^{13}$ Ωsq^{-1} to $\sim 1.8 \times 10^{11}$ Ωsq^{-1} . This also agrees with prior ensemble GO reduction studies [47].

All of these results thus indicate that the optical evolution observed in Region 1 stems from photoreduction of GO to rGO. At the single-sheet level, this is evidenced by a marked increase in absorption magnitude with a simultaneous quenching and blueshifting of GO's emission.

2.5 Single-rGO Sheet Absorption Microscopy/Spectroscopy

Having established that photoreduction of GO to rGO occurs in Region 1, we now use single-sheet absorption and emission measurements to characterize rGO. Two experimental approaches are used to produce rGO sheets in the following analysis: "stepwise" and "continuous" reduction methods. The stepwise method is outlined in Sect. 2.4 above. Briefly, the 405 nm reduction laser is interrupted every 0.5–2 s for an absorption measurement to be carried out. Continuous reduction, by contrast, entails exposing the GO sheet to continuous 405 nm laser light for 50–60 s before acquiring an absorption image [21]. The sheet is therefore at the end of Region 1 before reduction is interrupted.

Both methods result in identical optical behaviors throughout reduction. However, we find that continuous reduction always produces slightly more absorptive rGO sheets [21]. As an example, resulting continuous reduction rGO sheets possess a maximum absorption of ~ 1.7 %A at 520 nm. Stepwise reduction absorption values, by contrast, only reach ~ 1.3 %A at 520 nm [21]. An identical trend is seen for all wavelengths where continuous reduction results in more absorptive rGO sheets [21]. This suggests that reoxidation potentially occurs during stepwise reduction, lowering the final absorption magnitude of resulting rGO sheets [21].

Figure 2.11 shows representative single-layer rGO absorption images acquired at (a) 405 nm, (b) 520 nm, and (c) 640 nm on a sheet produced using the continuous reduction method. The sheet's %A-values are 2.1 % (405 nm), 1.7 % (520 nm), and 1.4 % (640 nm). Associated α -values are $\alpha_{405} = 2.1 \times 10^5$ cm⁻¹, $\alpha_{520} = 1.7 \times 10^5$ cm⁻¹, and $\alpha_{640} = 1.4 \times 10^5$ cm⁻¹. These numbers approach the graphene limit of 2.3 %A with a corresponding visible wavelength absorption coefficient of $\alpha = 5.8 \times 10^5$ cm⁻¹.

Similar to GO, sizable intrasheet absorption efficiency variations exist in rGO. In particular, Fig. 2.11c shows that a portion in the left center of the specific rGO

sheet probed absorbs more 640 nm light ($\sim 1.5\%$ A) than the lower half of the sheet ($\sim 1.4\%$ A). Figure 2.11a–c also shows corresponding single-sheet α -value distributions as green and blue histograms. They clearly contribute to ensemble rGO α -value distributions (Fig. 2.11a–c; top gray histograms, average of 12 rGO sheets) and illustrate inhomogeneous broadening effects due to sheet-to-sheet variations in their extent of oxidation.

Figure 2.11d shows the absorption spectrum of a stepwise-reduced rGO sheet (green triangles). Superimposed are average rGO %A-values that include values from

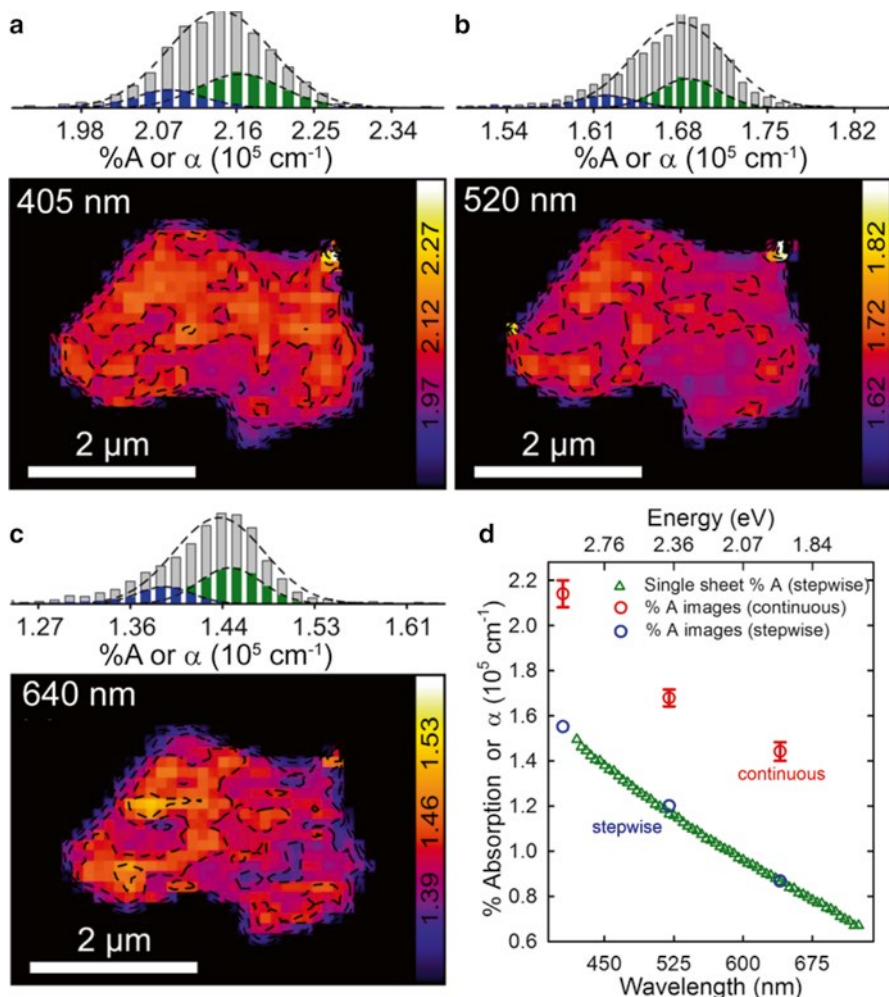


Fig. 2.11 Single-rGO sheet %A images for (a) 405 nm, (b) 520 nm, and (c) 640 nm light. rGO was produced for (a–c) using the continuous reduction method. (d) Absorption spectrum of an rGO sheet reduced using the stepwise method (green triangles) compared to %A-values obtained from images of rGO sheets prepared with stepwise (blue circles) and continuous (red circles) reduction methods

both continuous (red circles) and stepwise (blue circles) reduction methods. In each case, average %A-values are obtained by averaging 12 individual sheet absorption images. At this point, given our ability to acquire full, single-sheet rGO spectra, a fit to the single-sheet absorption data (green triangles) yields the following estimate of rGO's wavelength-dependent absorption coefficients between $\lambda=450\text{--}700\text{ nm}$:

$$\alpha\left(\text{cm}^{-1}\right)=4.42 \times 10^5-\lambda(1,160)+\lambda^2(1.39)-\lambda^3\left(7 \times 10^{-4}\right) . \quad (2.3)$$

2.6 GO Photoreduction Mechanism

We now address how GO reduces upon prolonged exposure to 405 nm light. In this regard, GO photoreduction is well documented in the literature. It is often attributed to a photothermal mechanism [17, 18, 48–50] wherein the absorption of light results in the eventual heating of the sample. This follows from the conversion of excess absorbed energy into thermal energy through non-radiative relaxation. What results are sizable temperature jumps, especially when there exists poor heat dissipation into the environment. Local heating then provides the necessary energy required to initiate thermal deoxygenation reactions in GO [48].

Supporting this, temperatures as high as 500 °C have been reported in GO samples exposed to high-power flashlamps [17]. Similarly, pulsed lasers in the ultraviolet [51–53], visible [51], and NIR [54, 55] have all been used to reduce GO. Their short pulses and high peak powers result in estimated sample temperatures exceeding 1,000 °C [53, 54]. Thus, the combination of rapid energy uptake and poor thermal transfer into the local environment leads to the photothermal reduction of GO.

In our study, though, we use relatively low-intensity ($I_{\text{exc}} \sim 220\text{--}380\text{ Wcm}^{-2}$) CW laser light to achieve GO reduction. A theoretical analysis—essentially an energy balance model based on known thermal conductance values and absorption strengths—provides a useful way to estimate GO's corresponding temperature rise (ΔT) [33, 56]. What results is

$$\Delta T = \frac{I_{\text{exc}} \left(\frac{\%A_{405}}{100} \right)}{h_{\text{sub}}} \quad (2.4)$$

where $\%A_{405}$ is the %A at 405 nm and h_{sub} is the interfacial thermal conductance between GO and SiO_2 . Since GO h_{sub} values are not available in the literature, we estimate it using values for graphene ($h_{\text{sub}} = 5 \times 10^7\text{ Wm}^{-2}\text{ K}^{-1}$) [57].

The model predicts ΔT -values of <1 K for single-layer GO exposed to 380 Wcm^{-2} of 405 nm CW excitation [33]. Consequently, resulting absolute temperatures are far below the $\sim 230\text{ }^\circ\text{C}$ temperatures needed to induce GO's thermal reduction [52]. Clearly, a photothermal mechanism alone does not account for the reduction seen in Fig. 2.9.

2.6.1 GO Photolysis

A handful of studies have implicated photolysis as an alternate, light-induced means of reducing GO [25, 49, 58]. In a photolytic mechanism, light is absorbed by a molecular resonance associated with an oxygen-containing functionality. The absorbed energy then dissipates through radiative or non-radiative channels or initiates a change in the chemical bond associated with the functionality. For GO, such changes include functional group migration and/or dissociation with theoretical activation energies (E_a) ranging from 0.28 to >1 eV [25, 58–61].

Specific GO functional group photolytic chemistries include direct OH, C–O–C, C=O, and COOH dissociation. Associated activation energies are 0.7 eV for OH [59], 1.9–2.1 eV for C–O–C [59, 62], and 3–4 eV for C=O and COOH groups [25, 58, 60]. Additional, more complicated, light-induced chemistries are also possible wherein multiple functional groups (primarily hydroxyls) interact to evolve H₂O (E_a ~0.28–0.46 eV) [61].

Functional group migration within GO's basal plane also occurs upon bond photolysis. In this case, hydroxyls (migration E_a ~0.32 eV) and epoxides (migration E_a ~0.9 eV) hop from carbon to carbon, leaving behind sp^2 hybridized carbons in their wake [61]. These groups eventually localize at defects/edges and subsequently dissociate through identical multiple functional group chemistries outlined above [25, 61].

All of these photolytic chemistries result in the evolution of H₂O, O₂, CO, and/or CO₂. This is consistent, with known products evolved during GO reduction [46]. Importantly, the release of water through either direct hydroxyl dissociation or through hydroxyl-hydroxyl interactions results in the reduction of GO without loss of carbon [61]. By contrast, other higher energy dissociation reactions, involving C–O–C/C=O/COOH, all result in carbon abstraction through CO and/or CO₂ emission [58]. This induces the breakdown of GO/rGO's basal plane carbon network and will be important for explaining GO's optical response in Region 2 [49].

For photolysis to be a plausible mechanism to explain the reduction of GO, however, the employed 405 nm (3.06 eV) excitation must be on resonance with oxygen-containing functional group transitions. Supporting this, highly oxidized GO ensembles show $n-\pi^*$ transitions between 400 and 420 nm [25]. Additionally, molecular-like transitions extending out as far as 550 nm have been observed in GO photoluminescence excitation (PLE) spectra [29]. The existence of these latter transitions is supported by density functional theory (DFT) calculations, suggesting that oxygen-functionalized sp^2 clusters exhibit electronic transitions throughout the visible spectrum [27].

To conduct an initial check on the likelihood of a photolytic reduction mechanism, single-GO sheet excitation wavelength-dependent studies were conducted. Single-layer specimens were exposed to identical intensities of 405, 520, and 640 nm light (I_{exc} ~700 Wcm⁻²) with the idea that photolytic reduction should not occur under prolonged red light illumination. Results of this study support the proposed photolytic mechanism. Namely, in the case of 640 nm excitation, an initial emission decay characteristic of Region 1 is essentially absent. Emission intensities

decrease by only ~10 % over the course of 1,800 s and no subsequent brightening is seen. These results suggest that the 640 nm excitation lies off-resonance with any ligand-related transition and agrees with prior ensemble absorption and PLE measurements [25, 29].

In stark contrast, both emission quenching and brightening are observed when individual GO sheets are exposed to 405 and 520 nm light. This is expected because both frequencies fall within the range of GO's oxygen-containing ligand resonances (400–550 nm) [25, 27, 29]. Furthermore, in the latter 520 nm case, this process occurs with kinetics that are ~5× slower, supporting the smaller abundance of these redder transitions [33]. Single-GO/rGO wavelength-dependent studies therefore qualitatively support a photolytic reduction mechanism.

2.6.2 Kinetics/Energetics of Photolysis

Given that GO's time-dependent absorption and emission trajectories (e.g., Fig. 2.9) are inherently linked to its photolytic reduction kinetics, photolytic rate constants can be extracted by analyzing absorption growth/emission decay traces. In Region 1, absorption traces (Fig. 2.9b) are empirically best fit with biexponential functions. A fast component contributes ~30 % to the total decay and has associated rate constants on the order of ~0.5 s⁻¹. A slow component also exists and accounts for ~70 % of the total decay. Associated rate constants are ~0.02 s⁻¹. To simplify subsequent analyses, rate constants from both contributions are combined into a single, weighted-average rate constant (k_a^1) [33, 21]. Region 1 emission decays are likewise analyzed with biexponential kinetics and yield weighted-average decay rate constants (k_e^1). Notably, k_a^1 and k_e^1 magnitudes are very similar, suggesting that both the absorption and emission evolve due to same physical process.

In Region 2, absorption decays are best described by single exponential functions. Consequently, a single k -value is extracted for the absorption (k_a^2). Emission growth trajectories are likewise fit with single exponential functions to give emission rate constants, k_e^2 . Extracted k_a^2 and k_e^2 values are on the order of ~2×10⁻³ s⁻¹ and 3×10⁻³ s⁻¹, respectively. Again, their magnitudes are similar and suggest that both absorption and emission changes in Region 2 arise from the same physical process. Furthermore, the magnitudes of Region 1 and Region 2 absorption/emission rate constants differ by 1–2 orders of magnitude, strongly suggesting that different chemistries lead to the diverging absorption/emission trends observed in Regions 1 and 2 of Fig. 2.9b [33, 21].

At this point, to link extracted k_a^1 and k_e^1 as well as k_a^2 and k_e^2 values to activation energies, temperature (T)-dependent photoreduction studies were conducted on individual GO sheets [33]. Sample temperatures ranging from 298 to 323 K were used with temperatures maintained with a resistively heated chamber and temperature controller (Lakeshore).

Results from these studies are shown in Fig. 2.12 where sheet-averaged Region 1/Region 2 rate constants, extracted from the T -dependent trajectories of several

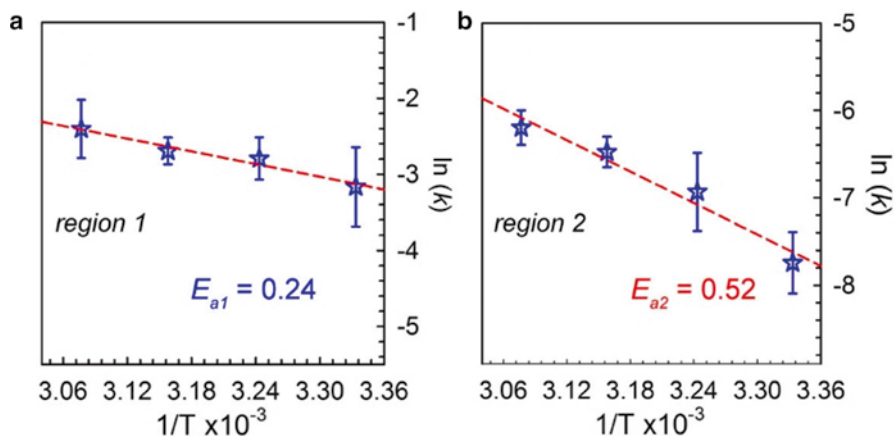
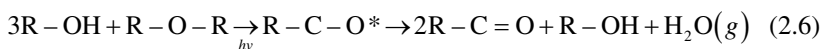
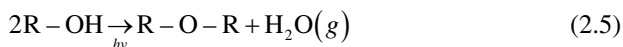


Fig. 2.12 Arrhenius plots of GO reduction kinetics for temperatures between 298 and 323 K for (a) *Region 1* and (b) *Region 2*. Error bars indicate the standard deviation in rate constant values for five individual GO sheets at a given T . Reprinted with permission from McDonald, M.P., et al., *Nano Letters*, 2013, 13, 5777–5784. Copyright 2013 American Chemical Society

different GO specimens, have been plotted as functions of temperature. Associated activation energies have subsequently been estimated using the Arrhenius relationship, where linear fits of experimental $\ln(k)$ versus $1/T$ give Region 1/Region 2 E_a -values of $E_{a1} \sim 0.24$ eV and $E_{a2} \sim 0.52$ eV, respectively [33]. Upper and lower bounds to these energies are $E_{a1} \sim 0.13$ – 0.39 eV and $E_{a2} \sim 0.33$ – 0.71 eV [33].

2.6.3 Photolytic Reduction Mechanism

Extracted E_{a1} and E_{a2} values enable us now to construct a more refined physical picture for the photolytic chemistries occurring in Regions 1, 2, and 3. Namely, the relatively small activation energies found in Region 1 ($E_{a1} \sim 0.13$ – 0.39 eV) suggest hydroxyl migration ($E_a \sim 0.32$ eV) as the dominant process responsible for GO reduction [61]. In this regard, we suggest that photolysis-induced OH migration leads to eventual OH localization at GO defects and edges whereupon corresponding increases of the local OH concentration enable multiple-functional group OH interactions to occur. This ultimately leads to the evolution of H_2O as well as the concomitant reduction of GO [61]. Such multiple-functional group reactions include [61]



where R represents the GO basal plane. Associated activation energies are 0.45 eV (Eq. 2.5) and 0.48 eV (step 1) as well as 0.30 eV (step 2) for Eq. (2.6).

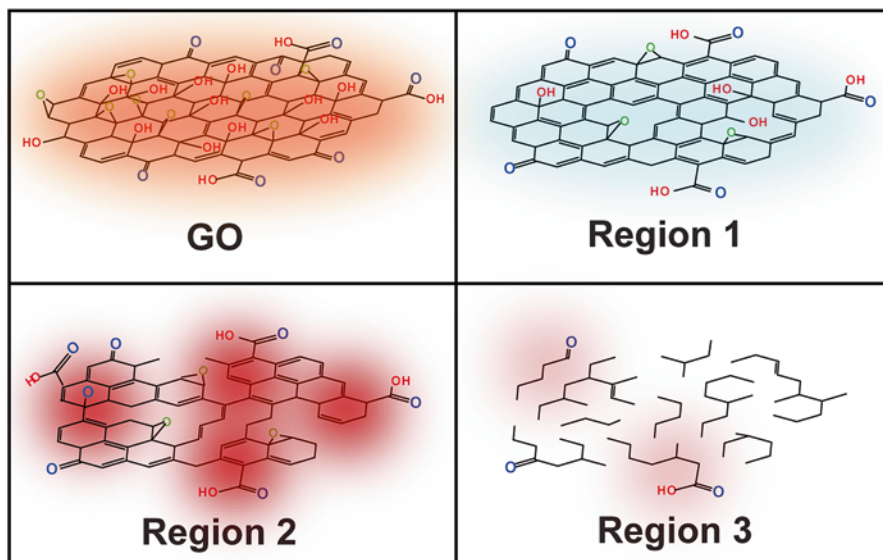


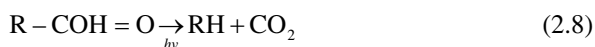
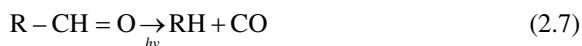
Fig. 2.13 Scheme depicting GO/rGO during each phase of its photolytic reduction

Other possible multiple functional group reactions exist and are described in more detail in ref. [61].

Since no carbon is lost in this phase, resulting rGO sheets consist of highly interconnected sp^2 domains. From an optical standpoint, what results is a weak, blueshifted emission spectrum for rGO, since an interconnected sp^2 network favors fast non-radiative recombination following photoexcitation [28]. In tandem, larger single-sheet absorption efficiencies result. This rationalizes why experimental %A values at the end of Region 1 approach the graphene limit of 2.3 %A [2, 21]. Figure 2.13 summarizes this by showing a schematic depiction of an rGO sheet at the end of Region 1.

The association of OH chemistries to Region 1's photoreaction mechanism is supported by ensemble mass spectrometry (MS) measurements, which show strong H_2O evolution during the initial stages of GO photolysis [46]. It is also supported by ensemble FTIR results shown in Fig. 2.10c where OH removal is clearly seen to occur during initial exposure to 405 nm radiation.

Region 2's larger E_a -values ($E_{a2} \sim 0.33\text{--}0.71$ eV) suggest that other photolytic processes simultaneously coexist with Region 1's OH chemistries. Based on known photolytic reactions, these chemistries likely involve direct OH dissociation (0.7 eV), C–O–C migration (0.9 eV), or even C–O–C/C=O/COOH dissociation (>1 eV). Most of these latter processes involve carbon abstraction through the evolution of CO and/or CO_2 [46, 49, 58]. This is illustrated in the following reactions [58]:



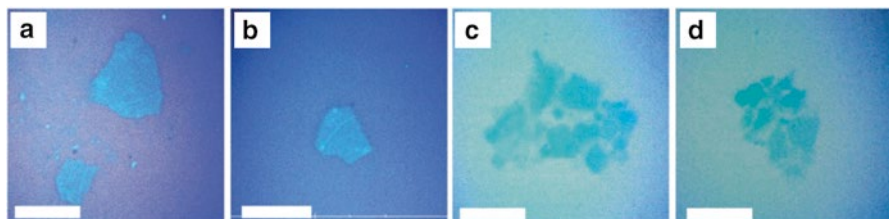


Fig. 2.14 Optical contrast images of GO on Si/SiO₂ (300 nm) substrates before (a, b) and after (c, d) 405 nm laser irradiation (2.8 Wcm^{-2} ; $\Phi = 2.1 \times 10^{23} \text{ photons/cm}^2$). Scale bars: 10 μm

where, again, R represents the GO basal plane. As with Region 1, our assignment is supported by ensemble MS studies, which show that CO and CO₂ are the primary products evolved during the final stages of GO photolysis [46]. It is also supported by Fig. 2.14 which shows optical contrast images of GO (a, b) and rGO in Region 2 (c, d). Apparent in the figures are clear morphological changes to rGO after extended 405 nm irradiation [33]. Holes and basal plane discontinuities are evident. This observation is also consistent with other AFM and TEM studies, which show the appearance of similar holes/defects in rGO following reduction [19, 49].

Optically, what results in Region 2 is a gradual loss of absorption due to carbon abstraction. rGO's emission, however, initially rises, since fragmentation of its aromatic network implies a loss of fast non-radiative recombination channels that induce emission quenching and blueshifts [28]. rGO's emission QY therefore increases and is accompanied by an apparent spectral redshift [28]. In essence, Region 2 unmasks the sp^2 domain size growth originally established in Region 1 with resulting near-isolated sp^2 /ligand clusters behaving as disparate, quasi-molecular entities. Corroborating this, fluorescence intermittency (reminiscent of quantum dot and single-molecule “blinking”) is apparent in Region 2 (Fig. 2.9b) [33].

The destructive nature of Region 2 photolytic chemistries also means that this state of rGO is only temporary. Continued photolysis results in additional carbon abstraction. This leads to continued absorption losses and, in the emission, ultimately results in irreversible photobleaching. The eventual photolytic destruction of rGO thus completes GO's optical life cycle and rationalizes its optical response in Region 3 of Fig. 2.9. Figure 2.13 summarizes this by providing a schematic description of rGO in Regions 2 and 3.

2.7 Temporal/Spatial Evolution of Photolysis

Having associated observed changes in GO's absorption/emission with photoreduction and having posited likely photolytic chemistries responsible for these changes, we now rationalize how GO's reduction spreads across its basal plane. This is done by analyzing sequential GO absorption and emission images acquired during photolysis. As seen earlier (e.g., Figs. 2.5, 2.6, and 2.8), significant optical heterogeneity exists

within individual GO sheets. We have attributed this to the existence of chemically segregated regions on the $\sim\mu\text{m}^2$ scale within GO's basal plane. What results are spatially heterogeneous reduction chemistries that can be observed in real time using single-sheet absorption and emission imaging. Corresponding analyses of spatially resolved emission quenching and absorption enhancements then lead to local estimates of GO reduction kinetics. In turn, these local rate constant variations allow us to rationalize the spatial evolution of GO's reduction, which empirically appears to "flow" across individual sheets after having nucleated at random reduction "hot spots."

In practice, spatially resolved, kinetic rate constant maps are constructed by analyzing trajectories associated with every pixel (a $250\text{ nm}\times 250\text{ nm}$ region) in an absorption/emission movie. Figure 2.9b shows one such representative trajectory. Region 1 and 2 absorption/emission fits are carried out using home-written software (a Java applet or a Visual Basic macro; source code available in refs. [33] and [21]). Region 3 analyses are omitted since we have previously attributed the kinetics here to the destruction of rGO.

Figure 2.15 shows resulting absorption (a, c) and emission (b, d) rate constant maps for a single GO sheet undergoing photoreduction (the same sheet featured in Fig. 2.9a). Region 1 absorption/emission maps are shown in the left column. Corresponding Region 2 absorption/emission maps are shown in the right column. In all cases, clear intrasheet k_a/k_e variations are apparent. For example, the absorption growth (k_a^1) rate map in Fig. 2.15a shows a large area in the upper right-hand corner of the sheet with $k_a^1 \sim 0.16\text{ s}^{-1}$. A second section in the bottom left of the sheet shows $k_a^1 \sim 0.06\text{ s}^{-1}$. Similar heterogeneities are present in other maps.

As expected from our discussion in Section 2.6.3, the analysis reveals spatial correlations between k_a and k_e rate constants within a given Region. To illustrate, in Region 1 a high- k ridge exists in the upper right-hand portion of both Fig. 2.15a ($k_a^1 \sim 0.16\text{ s}^{-1}$) and Fig. 2.15b ($k_e^1 \sim 0.07\text{ s}^{-1}$). Other correlations between k_a^1 and k_e^1 are evident in both the middle and bottom right sections of the same sheet. In Region 2, analogous absorption/emission k -value correlations exist. For example, the bottom right protrusion in Fig. 2.15c, d exhibits similarly peaked k_a^2 and k_e^2 values.

Furthermore, as seen earlier, extracted absorption/emission rate constants for a given region take the same order of magnitude. Specifically, average Region 1 absorption/emission rate constants in Fig. 2.15 are $\langle k_a^1 \rangle = 0.10\text{ s}^{-1}$ and $\langle k_e^1 \rangle = 0.04\text{ s}^{-1}$. In Region 2 they are $\langle k_a^2 \rangle = 1.75 \times 10^{-3}\text{ s}^{-1}$ and $\langle k_e^2 \rangle = 3.8 \times 10^{-3}\text{ s}^{-1}$. The good agreement between these k_a and k_e pairs then suggests that, within a given region, changes in the absorption and emission arise from the same physical process. Differing magnitudes of Region 1/Region 2 k_a/k_e values simultaneously suggest different photolytic chemistries being responsible for the behavior in these regions.

Proposed Region 1 and Region 2 photolytic chemistries have been outlined in Section 2.6.3 by linking rate constants to activation energies using temperature-dependent measurements. Within the context of the spatially resolved measurements described here, this leads to analogous E_a maps constructed from k_a/k_e maps shown in Fig. 2.15. At this point, the most important thing to note is that in Region 1 of Fig. 2.15, peaks in the rate constant map are associated with the smallest activation

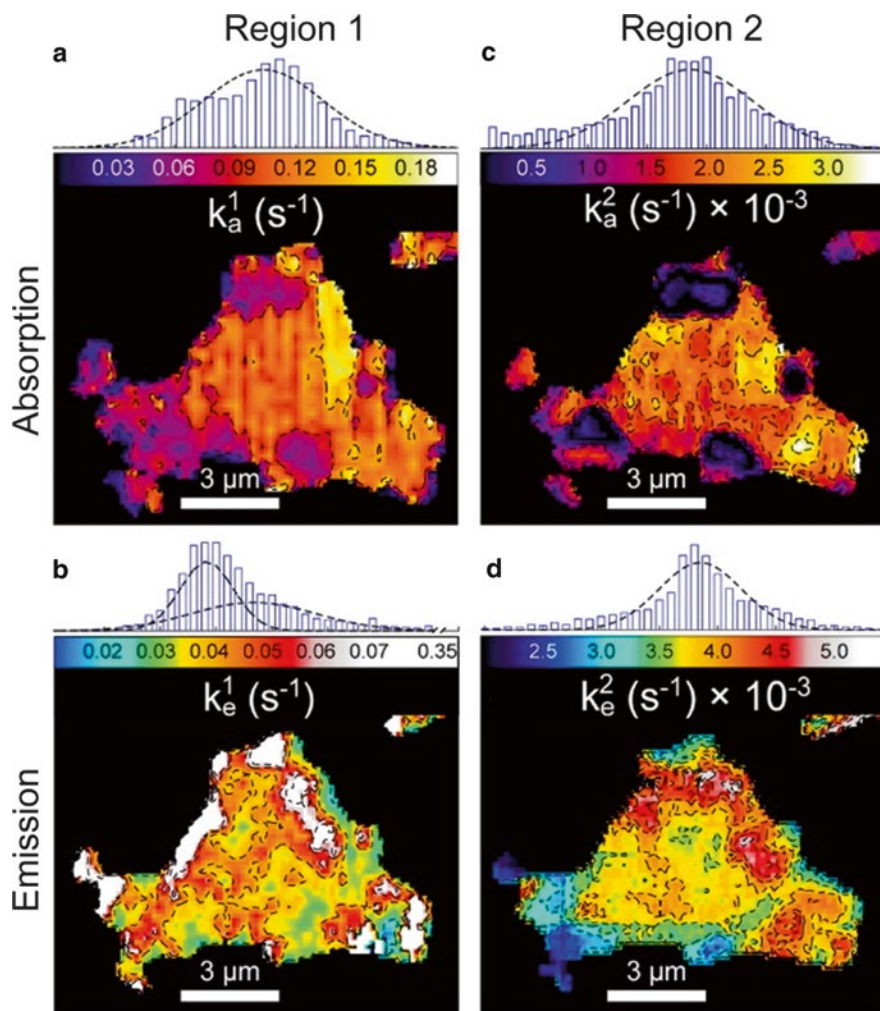


Fig. 2.15 Absorption (at 520 nm) and emission rate constant maps obtained for (a, b) *Region 1* and (c, d) *Region 2*. *Histograms* illustrate absorption/emission rate constant distributions present within the GO sheet. Reprinted with permission from Sokolov, D.A., et al., *Nano Letters* 2014, 14, 3172–3179. Copyright 2014 American Chemical Society

energies ($E_a \sim 0.20$ eV). It is these very regions which “nucleate” reduction in GO photolytic absorption/emission movies.

Given that we have previously attributed GO reduction in Region 1 to OH photolytic chemistries and specifically to OH migration and multiple OH group reactions (Eqs. 2.5 and 2.6) [61], this suggests that GO reduction commences in regions of the basal plane possessing relatively large OH concentrations. Once nucleated, reduction “spreads” outwards since photolytic reduction in neighboring regions, with fewer

OH groups, involves OH migration to local defects/edges followed by multiple OH group chemistries, which ultimately lead to the evolution of water. From a kinetic standpoint, what results is an effective activation energy/rate constant that is larger/smaller than at nucleation sites due to the fact that multiple processes are involved in GO reduction in these locations. This suggests that the spatially heterogeneous rate constant/activation energy maps seen in Fig. 2.15 reflect the large-scale distribution of OH functional groups within GO's basal plane.

Some evidence for this hypothesis exists. Namely, the absorption growth/emission decay traces in Region 1 are best fit to biexponential functions. The non-single exponential nature of these traces thus implies that not one but rather several photolytic processes underlie the observed kinetics. Thus, there exists a need for future experiments that can better unravel the various, unresolved, photolytic processes present in Region 1. Furthermore, a need exists for experiments that possess spatially resolved chemical specificity and which can better assess large-scale functional group distributions in GO/rGO.

At this point, an analysis of Region 2 kinetics is more complicated. However, similar "nucleation" and photolysis fronts are seen in Region 2 photoreduction movies. Our prior analysis of the kinetics here has suggested that carbon-abstracting photolytic chemistries are at play (Eqs. 2.7 and 2.8). Hence, the rGO produced in Region 1 continues to be reduced in Region 2 and, in tandem, undergoes gradual breakdown of its sp^2 network.

To explain the visual propagation of Region 2 photolytic chemistries, we first posit that these latter chemistries begin in aromatic sp^2 domain-rich regions. In principle, a correlation could exist between nucleation sites in Regions 1 and 2 provided that OH-rich regions produce large, strongly absorbing sp^2 domains when reduced. However, in practice, this need not be the case. At present, the data is ambiguous and hence spatial correlations between Region 1 and 2 nucleation sites cannot be established.

Next, in sections of individual rGO sheets containing strongly absorbing sp^2 domains, associated photolytic processes propagate due to temperature gradients that exist between these domains and neighboring sp^3 hybridized regions. In this regard, given that semi-isolated sp^2 clusters are more absorptive than their sp^3 surroundings and have modest emission quantum yields, excitation of these clusters leads to local heating. What results are ΔT gradients of up to ~ 4 K based on the energy balance model discussed earlier (Eq. 2.4) [33]. While this temperature increase is not enough to directly induce thermal reduction, it can enhance the rate of an activated process through local variations of the chemical rate constant. As an illustration, rate constant increases of 20–45 % are possible when activation energies are in the range of $E_a \sim 0.52$ –70 eV [33]. Consequently, partially oxidized sp^3 -rich domains in close proximity to strongly absorbing and "hot" sp^2 regions should undergo photolytic chemistries faster than more isolated sp^3 domains. Thus, with continued reduction leading to corresponding increases in sp^2 domain number as well as size, a ΔT - k feedback loop ensues, causing the photolysis front to spread and eventually consume the entire rGO sheet.

2.8 Conclusions

GO and rGO have been studied extensively using various structural and chemical microscopies. They have also been studied extensively using ensemble absorption and emission spectroscopies. Recently, a growing number of atomic resolution microscopies have probed the structural and electronic properties of these materials. However, to date, little work has been done to understand their photophysics at the microscopic level. A number of reasons exist for wanting to do this. Perhaps the most pressing involves a desire to develop a deeper understanding of GO's photoreduction mechanism.

In what has preceded, we have described work to study the optical response of individual single-layer GO and rGO using spatially resolved absorption and emission microscopies/spectroscopies. We find significant spatial and spectral heterogeneities within the optical response of individual GO and rGO sheets. The origin of these absorption and emission heterogeneities likely stems from the presence of varying-sized sp^2 domains as well as chemical disorder within GO's basal plane. The single-sheet microscopies/spectroscopies we have developed are quantitative. Consequently, we have established the first experimental accounting of GO and rGO absorption parameters across the visible.

More intriguingly, under prolonged illumination with 405 nm light, dynamics in the optical response of single-layer GO are seen. Namely, an apparent emission quenching and spectral blueshifting are observed. In tandem, a noticeable increase of the absorption occurs. Afterwards, the absorption decreases while the emission increases markedly and is accompanied by a sizable redshift of the spectrum. Finally, the end of GO's optical life cycle is characterized by a continued loss of absorption along with apparent emission intermittency prior to irreversible photobleaching.

By linking various ensemble and single-sheet experiments, we have established that GO reduction to rGO is characterized by aforementioned emission quenching and absorption growth, seen in the initial stages of GO's optical life cycle. The underlying mechanism responsible for this photoreduction is thought to be photolytic in nature—not photothermal. Specifically, energy balance estimates show that only modest temperature jumps are achieved in GO following the absorption of light. Detailed kinetics studies on GO's spatially resolved absorption and emission dynamics subsequently establish rate constants and associated activation energies consistent with known OH photolytic chemistries. Consequently, we attribute observed spatially heterogeneous GO reduction chemistries to photolytic OH processes and, by the same token, to large-scale OH concentration variations across GO's basal plane.

Prolonged illumination leads to the eventual destruction of rGO. This occurs through additional, carbon-abstracting photolytic chemistries that follow GO's photoreduction. Initially, these processes result in rGO's apparent emission brightening. Their destructive nature, though, appears through commensurate absorption losses. Beyond a certain point, continued photolysis leads to the physical destruction of rGO

as observed optically through complete loss of its absorption along with irreversible photobleaching. This is also seen structurally through unambiguous morphological changes in optical images of rGO after prolonged illumination and in corresponding AFM and TEM measurements. The role of these latter photolytic processes has again been established using detailed, spatially resolved kinetic studies on rGO wherein we find observed rate constants and associated activation energies consistent with those of known carbon-abstracting photolytic chemistries.

We have therefore constructed a detailed, microscopic picture of GO's optical properties. However, there are still a number of unresolved questions within the field. For example, the origin of GO's emission is still debated. Evidence in the literature suggests that it can arise from direct recombination in sp^2 clusters, quasi-molecular ligand/ sp^2 states, or other photophysical processes. Unfortunately, the optical approach illustrated in this chapter is limited to a ~ 200 nm resolution, and is thus unable to interrogate individual sp^2 domains. An intriguing possibility for overcoming this limitation could be realized through single-GO/rGO sheet near-field scanning optical microscopy.

The measurements outlined in this chapter have also established unprecedented insight into GO's photoreduction mechanism. In turn, these results provide the foundation for future studies aiming to better understand light-initiated GO-to-rGO interconversion. Beyond this, these studies and others like them may reveal opportunities for better controlling GO's reduction, ultimately enabling spatially selective patterning and hence local control of GO's optical and electrical properties. Future spectroscopic studies that elucidate the reversibility and fidelity of these photochemical processes are thus crucial to next-generation GO/rGO device fabrication. Finally, the developed absorption/emission techniques discussed here open up opportunities for studying the optical properties of other two-dimensional systems in ways free of constraints limiting existing, emission-based single-particle microscopies.

Acknowledgements MK thanks the ACS PRF (Type ND 51675) and the Army Research Office (W911NF-12-1-0578) for financial support. JHH thanks CONICET for the international cooperation funds [D979 (25-03-2013)], FONCyT for research grant P.BID2012 PICT-2041, and University of Buenos Aires for grants UBACYT 2015-2017 20020130100643BA and UBACYT 01-w971.

References

1. Novoselov KS, Geim AK, Morozov SV et al (2004) Electric field effect in atomically thin carbon films. *Science* 306:666–669
2. Nair RR, Blake P, Grigorenko AN et al (2008) Fine structure constant defines visual transparency of graphene. *Science* 320:1308
3. Hwang EH, Adam S, Das Sarma S (2007) Carrier transport in two-dimensional graphene layers. *Phys Rev Lett* 98:186806-1–186806-4
4. Wu Z-S, Ren W, Gao L et al (2009) Synthesis of graphene sheets with high electrical conductivity and good thermal stability by hydrogen arc discharge exfoliation. *ACS Nano* 3: 411–417

5. Balandin AA, Ghosh S, Bao W et al (2008) Superior thermal conductivity of single-layer graphene. *Nano Lett* 8:902–907
6. Kim KS, Zhao Y, Jang H et al (2009) Large-scale pattern growth of graphene films for stretchable transparent electrodes. *Nature* 457:706–710
7. Wang X, Ouyang Y, Li X et al (2008) Room-temperature all-semiconducting sub-10-nm graphene nanoribbon field-effect transistors. *Phys Rev Lett* 100:206803-1–206803-4
8. Chae SJ, Gunes F, Kim KK et al (2009) Synthesis of large-area graphene layers on poly-nickel substrate by chemical vapor deposition: wrinkle formation. *Adv Mater* 21:2328–2333
9. Emtsev KV, Bostwick A, Horn K et al (2009) Towards wafer-size graphene layers by atmospheric pressure graphitization of silicon carbide. *Nat Mater* 8:203–207
10. Zhang Y-L, Guo L, Xia H et al (2014) Photoreduction of graphene oxides: methods, properties, and applications. *Adv Opt Mater* 2:10–28
11. Brodie BC (1859) On the atomic weight of graphite. *Philos Trans R Soc Lond* 149:249–259
12. Hummers WS, Offeman RE (1958) Preparation of graphitic oxide. *J Am Chem Soc* 80:1339–1339
13. Lorf A, He H, Forster M et al (1998) Structure of graphite oxide revisited. *J Phys Chem B* 102:4477–4482
14. Krishnan D, Kim F, Luo J et al (2012) Energetic graphene oxide: challenges and opportunities. *Nano Today* 7:137–152
15. Stankovich S, Dikin DA, Piner RD et al (2007) Synthesis of graphene-based nanosheets via chemical reduction of exfoliated graphite oxide. *Carbon* 45:1558–1565
16. Wang X, Zhi L, Müllen K (2008) Transparent, conductive graphene electrodes for dye-sensitized solar cells. *Nano Lett* 8:323–327
17. Gilje S, Dubin S, Badakhshan A et al (2010) Photothermal deoxygenation of graphene oxide for patterning and distributed ignition applications. *Adv Mater* 22:419–423
18. Sokolov DA, Shepperd KR, Orlando TM (2010) Formation of graphene features from direct laser-induced reduction of graphite oxide. *J Phys Chem Lett* 1:2633–2636
19. Erickson K, Erni R, Lee Z et al (2010) Determination of the local chemical structure of graphene oxide and reduced graphene oxide. *Adv Mater* 22:4467–4472
20. Paredes JI, Villar-Rodil S, Solis-Fernandez P et al (2009) Atomic force and scanning tunneling microscopy imaging of graphene nanosheets derived from graphite oxide. *Langmuir* 25:5957–5968
21. Sokolov DA, Morozov YV, McDonald MP et al (2014) Direct observation of single layer graphene oxide reduction through spatially resolved, single sheet absorption/emission microscopy. *Nano Lett* 14:3172–3179
22. Zhou Y, Bao Q, Varghese B et al (2010) Microstructuring of graphene oxide nanosheets using direct laser writing. *Adv Mater* 22:67–71
23. Eda G, Lin Y-Y, Mattevi C et al (2010) Blue photoluminescence from chemically derived graphene oxide. *Adv Mater* 22:505–509
24. Shang J, Ma L, Li J et al (2012) The origin of fluorescence from graphene oxide. *Sci Rep* 2:792-1–792-8
25. Andryushina NS, Stroyuk OL, Dudarenko GV et al (2013) Photopolymerization of acrylamide induced by colloidal graphene oxide. *J Photochem Photobiol A* 256:1–6
26. Li D, Muller MB, Gilje S et al (2008) Processable aqueous dispersions of graphene nanosheets. *Nat Nanotechnol* 3:101–105
27. Chien C-T, Li S-S, Lai W-J et al (2012) Tunable photoluminescence from graphene oxide. *Angew Chem Int Ed* 51:6662–6666
28. Exarhos AL, Turk ME, Kikkawa JM (2013) Ultrafast spectral migration of photoluminescence in graphene oxide. *Nano Lett* 13:344–349
29. Galande C, Mohite AD, Naumov AV et al (2011) Quasi-molecular fluorescence from graphene oxide. *Sci Rep* 1:85-1–85-5
30. Luo Z, Vora PM, Mele EJ et al (2009) Photoluminescence and band gap modulation in graphene oxide. *Appl Phys Lett* 94:111909-1–111909-3

31. Loh KP, Bao Q, Eda G et al (2010) Graphene oxide as a chemically tunable platform for optical applications. *Nat Chem* 2:1015–10024
32. Gokus T, Nair RR, Bonetti A et al (2009) Making graphene luminescent by oxygen plasma treatment. *ACS Nano* 3:3963–3968
33. McDonald MP, Eltom A, Vietmeyer F et al (2013) Direct observation of spatially heterogeneous single-layer graphene oxide reduction kinetics. *Nano Lett* 13:5777–5784
34. Cuong TV, Pham VH, Tran QT et al (2010) Photoluminescence and raman studies of graphene thin films prepared by reduction of graphene oxide. *Mater Lett* 64:399–401
35. Chen J-L, Yan X-P (2010) A dehydration and stabilizer-free approach to production of stable dispersion of graphene nanosheets. *J Mater Chem* 20:4328–4332
36. Hou X-L, Li J-L, Drew SC et al (2013) Tuning radical species in graphene oxide in aqueous solution by photoirradiation. *J Phys Chem C* 117:6788–6793
37. Li J-L, Kudin KN, McAllister MJ et al (2006) Oxygen-driven unzipping of graphitic materials. *Phys Rev Lett* 96:176101-1–176101-4
38. Giblin J, Vietmeyer F, McDonald MP et al (2011) Single nanowire extinction spectroscopy. *Nano Lett* 11:3307–3311
39. Vietmeyer F, McDonald MP, Kuno M (2012) Single nanowire microscopy and spectroscopy. *J Phys Chem C* 116:12379–12396
40. McDonald MP, Vietmeyer F, Kuno M (2012) Direct measurement of single CdSe nanowire extinction polarization anisotropies. *J Phys Chem Lett* 3:2215–2220
41. Vietmeyer F, Tchelidze T, Tsou V et al (2012) Electric field-induced emission enhancement and modulation in individual CdSe nanowires. *ACS Nano* 6:9133–9140
42. McDonald MP, Vietmeyer F, Aleksuk D et al (2013) Supercontinuum spatial modulation spectroscopy: detection and noise limitations. *Rev Sci Instrum* 84:113104-1–113104-7
43. Geim AK, Novoselov KS (2007) The rise of graphene. *Nat Mater* 6:183–191
44. Dreyer DR, Park S, Bielawski CW et al (2010) The chemistry of graphene oxide. *Chem Soc Rev* 39:228–240
45. Chen W, Yan L (2010) Preparation of graphene by a low-temperature thermal reduction at atmosphere pressure. *Nanoscale* 2:559–563
46. Shulga YM, Martynenko VM, Muradyan VE et al (2010) Gaseous products of thermo- and photo-reduction of graphite oxide. *Chem Phys Lett* 498:287–291
47. Eda G, Fanchini G, Chhowalla M (2008) Large area ultrathin films of reduced graphene oxide as a transparent and flexible electronic material. *Nat Nanotechnol* 3:270–274
48. Cote LJ, Cruz-Silva R, Huang J (2009) Flash reduction and patterning of graphite oxide and its polymer composite. *J Am Chem Soc* 131:11027–11032
49. Matsumoto Y, Koinuma M, Ida S et al (2011) Photoreaction of graphene oxide nanosheets in water. *J Phys Chem C* 115:19280–19286
50. Guo H, Peng M, Zhu Z et al (2013) Preparation of reduced graphene oxide by infrared irradiation induced photothermal reduction. *Nanoscale* 5:9040–9048
51. Abdelsayed V, Moussa S, Hassan HM et al (2010) Photothermal deoxygenation of graphite oxide with laser excitation in solution and graphene-aided increase in water temperature. *J Phys Chem Lett* 1:2804–2809
52. Sokolov DA, Rouleau CM, Geohegan DB et al (2013) Excimer laser reduction and patterning of graphite oxide. *Carbon* 53:81–89
53. Huang L, Liu Y, Ji L-C et al (2011) Pulsed laser assisted reduction of graphene oxide. *Carbon* 49:2431–2436
54. Trusovas R, Ratautas K, Raciukaitis G et al (2013) Reduction of graphite oxide to graphene with laser irradiation. *Carbon* 52:574–582
55. Zhang Y, Guo L, Wei S et al (2010) Direct imprinting of microcircuits of graphene oxides film by femtosecond laser reduction. *Nano Today* 5:15–20
56. Wang D, Carlson MT, Richardson HH et al (2011) Absorption cross section and interfacial thermal conductance from an individual optically excited single-walled carbon nanotube. *ACS Nano* 5:7391–7396

57. Jeong H-K, Lee YP, Jin MH et al (2009) Thermal stability of graphite oxide. *Chem Phys Lett* 470:255–258
58. Plotnikov VG, Smirnov VA, Alfimov MV et al (2011) The graphite oxide photoreduction mechanism. *High Energy Chem* 45:411–415
59. Lahaye RJWE, Jeong HK, Park CY et al (2009) Density functional theory of graphite oxide for different oxidation levels. *Phys Rev B* 79:125435-1–125435-8
60. Smirnov VA, Shul'ga YM, Denisov NN et al (2012) Photoreduction of graphite oxide at different temperatures. *Nanotechnol Russia* 7:156–163
61. Ghaderi N, Paressi M (2010) First-principle study of hydroxyl functional groups on pristine, defected graphene, and graphene epoxide. *J Phys Chem C* 114:21625–21630
62. Sorescu DC, Jordan KD (2001) Theoretical study of oxygen adsorption on graphite and the (8,0) single-walled carbon nanotube. *J Phys Chem B* 105:11227–11232